



Effect of temperature gradient on composition and morphology of synthetic chlorine-containing biomass boiler deposits

Daniel Lindberg ^{*}, Jonne Niemi, Markus Engblom, Patrik Yrjas, Tor Laurén, Mikko Hupa

Åbo Akademi University, Johan Gadolin Process Chemistry Centre, Biskopsgatan 8, 20500 Turku, Finland

ARTICLE INFO

Article history:

Received 31 March 2015

Received in revised form 29 September 2015

Accepted 3 October 2015

Available online 21 October 2015

Keywords:

Temperature gradient

Superheater deposit

Molten salt

Alkali chloride

Computational fluid dynamics

ABSTRACT

A novel laboratory method has been developed to study the chemical and physical behavior of ash deposits in a temperature gradient. Experiments with synthetic alkali salt mixtures similar to biomass boiler deposits show that alkali chlorides evaporate from hotter particles in the deposit and condense on colder particles closer to the cooled metal surface or even condense on the metal surface. Formation of a partially or completely molten layer in the outer hotter region closer to the flue gas is also observed in the experiments.

The effect of time is shown to be significant for the enrichment of chlorides as longer experiment time leads to higher amounts of vaporization, transport and condensation within the deposits.

These effects are quantitatively verified using Computational Fluid Dynamics modeling.

The transport of alkali chloride vapors becomes negligible if the deposit and metal temperature is cold enough. An enrichment of alkali chlorides towards the cooled metal surface occurs and can increase chlorine-induced corrosion of superheaters as the deposits mature over time.

The experimental observations are similar to superheater deposit morphologies observed in biomass boilers, such as straw-fired grate boilers.

© 2015 Elsevier B.V. All rights reserved.

1. Introduction

Fireside corrosion is an important reason for costly unscheduled shut-downs of biomass-fired boilers [1]. Corrosion of superheater materials is often connected to the presence of corrosive deposits and especially the presence of a molten phase at the alloy/deposit interface can lead to severe corrosion [2,3]. Steam temperatures in superheaters are often kept below the first melting temperature of the deposits to minimize the risk of severe corrosion [4–6]. However, it has been shown that corrosion of superheater materials may also occur even if a molten phase is not in contact with the superheater material surface, for example if the deposit contains chlorides [1,7–9]. Skrifvars et al. [7,8] showed in laboratory corrosion tests that high nickel alloys had good corrosion resistance to chloride-containing deposits at temperatures below the first melting temperature of the deposit, whereas low-alloyed and austenitic steels were corroded if the deposit contained small amounts of chlorine, even at subsolidus conditions.

Typically, the main ash-forming elements in various biomass fuels are Ca, K, Si, and Mg [10–12] but fast growing energy crops or different agricultural residues, such as wheat straw, can contain high levels of Cl, S, and P. The presence of chlorine in the ash deposits is problematic due to the formation of low-melting mixtures containing metal chlorides.

Straw-fired grate boilers often exhibit heat exchanger deposits containing high amounts of KCl and K₂SO₄ with minor amounts of Ca- and Si-compounds, such as K-silicates and Ca-silicates [13,14]. The first-melting temperature for KCl + K₂SO₄ mixtures is 690 °C [4] but the addition of Na-compounds, such as NaCl or Na₂SO₄, or corrosion products, such as K₂CrO₄ or FeCl₂, may lower the first-melting temperature of the deposit by several hundred degrees [1].

Superheater deposits in black liquor recovery boilers consist mainly of Na₂SO₄, Na₂CO₃, and NaCl with minor amounts of corresponding K-compounds [15]. Na and S originate from the cooking chemicals in the pulping process, whereas K and Cl are non-process elements mainly originating from the wood raw material. The deposits typically have first melting temperatures between 500 and 600 °C.

Biomass boilers firing woody biomass fuels tend to have less problematic superheater deposits compared to the straw-fired boilers, due to lower ash contents and lower levels of Cl. However, fuel mixtures containing waste fractions, such as waste wood or municipal solid waste, are highly problematic due to the presence of heavy metals, such as Zn and Pb. Deposits containing PbCl₂ or ZnCl₂ can melt at temperatures as low as 300 °C [16,17].

Hansen et al. [13] and Jensen et al. [18] have studied the detailed composition and morphology of superheater deposits from straw-fired grate boilers. Hansen et al. [13] studied both deposits from air-cooled probes and mature deposits sampled directly from the boiler. The mature deposits showed a characteristic layered structure parallel with the metal surface of the superheater. Six layers were observed and were

^{*} Corresponding author.

E-mail address: Daniel.lindberg@abo.fi (D. Lindberg).

as follows starting with the innermost layer next to the metal surface: a) Fe/Cr oxide layer; b) dense K_2SO_4 with small inclusions of Fe-oxide; c) porous layer of KCl; d) dense layer of KCl; e) dense layer of KCl with inclusions of ash particles; f) porous layer consisting of sintered fly ash particles containing Ca and Si. The two innermost layers were up to 100 μm thick, whereas the four outer layers were several millimeters thick. The probe deposits consisted of an inner layer of KCl and an outer layer of sintered fly ash. Jensen et al. [18] observed a similar structure of the superheater deposits with three main layers. The inner layer consisted of several sublayers with a Fe-oxide scale next to the superheater covered by a dense layer mainly consisting of K_2SO_4 , followed by a porous layer of KCl flakes and then a dense layer of mainly KCl. The intermediate layer consisted of dense KCl with inclusions of silicate and Ca-rich particles. The outermost layer was very porous, consisting mainly of Si- and Ca-rich particles glued together by molten KCl and K_2SO_4 . The reported steam temperatures were 400–500 °C and the flue gas temperatures were around 900–1000 °C. Based on the SEM images, some of the inner layers in the deposit had not experienced temperatures above the melting temperature of KCl (771 °C) or the solidus temperature of KCl + K_2SO_4 mixtures (690 °C), whereas the outer layers showed evidence of being molten at some point in time.

The temperature gradient from the superheater material through the deposit to the flue gas can be several hundred degrees Celsius. A schematic picture of the temperature profile of a heat exchanger/deposit cross-section is shown in Fig. 1 [19].

The maximum steam temperature in the superheater of a biomass boiler is typically around 500 °C. At the steel/deposit interface, the temperature is slightly higher. In an ideal case, the first melting temperature, also called T_0 , of the deposit is higher than the temperature at the steel/deposit interface in order to reduce corrosion risks. Assuming a chemically homogenous deposit and steady-state conditions, the T_0 isotherm will be at a fixed distance from the steel/deposit surface. The melt fraction will increase towards the flue gas side of the cross-section. In case the deposit is situated on a vertical surface, the partially molten deposit will tend to flow downwards when the melt fraction is high enough

or viscosity of the molten phase is low enough. A melt fraction of 70% on mass basis is a commonly used criterion for alkali salt deposits, and the corresponding temperature is called the flow temperature or T_{70} [19–21].

Many laboratory test setups for studying ash-related high-temperature corrosion in combustion environments have been developed for isothermal conditions [7,8,22,23]. Real or synthetic ash deposits are either applied on a steel or alloy sample, or the steel is inserted in a salt sample and subsequently inserted in a furnace at a fixed temperature and standard time. However, in boiler environments, the superheater material and the deposit are exposed to a temperature gradient that can be several hundred degrees Celsius going from the steam in the superheater, through the steel and the deposit to the hot flue gas.

Only a few experimental setups have been reported for ash-related corrosion with a thermal gradient over the superheater material and deposit. Lagerbom et al. [24], Kawahara [25] and Brossard et al. [26] have developed laboratory test setups for studying the corrosion of superheater materials in temperature gradients. Only Lagerbom et al. [24] reported details of the deposit properties. The alloy samples were carbon steel (13CrMo4–5) and a nickel based super alloy (Alloy 625), and the deposits were mixtures of Na_2SO_4 , K_2SO_4 , NaCl, and KCl. The sample temperature was between 470 and 560 °C, and the gas temperature in the furnace was between 700 and 800 °C. They observed that the deposits were segregated in to two or three distinct layers during the experiments. If the sample temperature was low, the deposit layer closest to the metal was similar to the original salt mixture. The upper layer had the composition of a predicted molten phase of the partly molten bulk composition and the intermediate layer had the composition of the predicted solid phase. The lowest layer was not present if the sample temperature was above the first-melting temperature of bulk composition.

It is clear from the study of Lagerbom et al. [24] that the physical and chemical properties of the deposit change over time in a thermal gradient. Some of the changes may be related to sintering dependent on local temperature [27], vaporization/condensation of volatile species, phase separation connected to the formation of a melt, and the thermal diffusion process called the Soret effect [28], where an initially homogenous system evolves a composition gradient under the thermal gradient. However, this effect occurs mainly in homogenous phases, such as aqueous solutions or melts.

Lindberg et al. [29] developed a novel laboratory method to study the effect of temperature gradients on deposit chemistry and morphology, as well as superheater steel corrosion. Different alkali salt mixtures were studied. The temperature of the deposit/steel interface was set to 400 °C or 500 °C and a deposit layer with an initial thickness of about 5 mm was applied on steel rings. The furnace temperature was set to 980 °C but the measured temperature just above the deposit surface was about 800 °C. A eutectic mixture of NaCl + Na_2SO_4 with a first melting temperature of 626 °C, showed the formation of a eutectic layer towards the hot region of the furnace, whereas the colder part remained as a porous layer. Migration of NaCl was observed in the porous layer, with alkali chloride transport from the hot region towards colder regions within the porous layer. Condensation of pure chloride on deposit particles was observed and the condensation layer thickness decreased towards the metal surface. Experiments were also made for synthetic black liquor recovery boiler deposits, which are rich in Na_2SO_4 with minor amounts of NaCl, KCl, and K_2SO_4 . Enrichment of chloride close to the deposit/steel interface was also observed. The chloride enrichment was probably due to enrichment of a chloride-rich molten phase as the whole deposit was completely sintered due to the low first melting temperature (around 520–530 °C). The corrosion of the steels in the experiments was similar to experiments performed at isothermal conditions.

The objective of the present study was to investigate the effect of the melting properties on the morphology of synthetic deposits with compositions similar to black liquor recovery boiler deposits (NaCl + Na_2SO_4

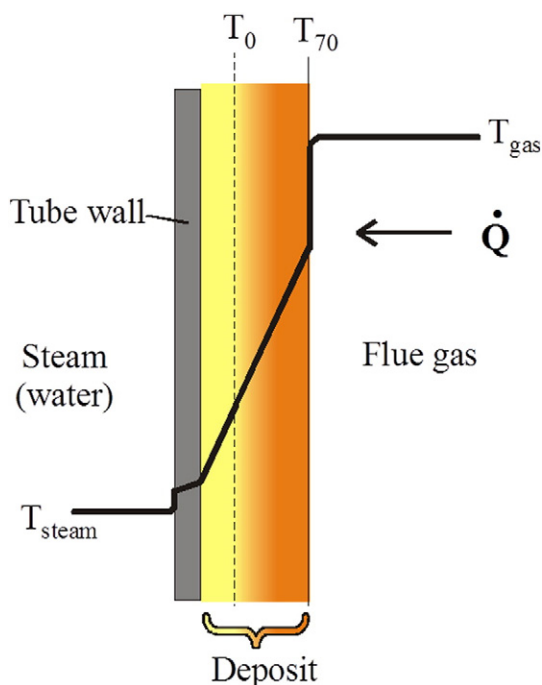


Fig. 1. Schematic picture of a cross-section of a superheater tube and deposit. The schematic temperature profile is shown with the black line, where the temperature is qualitatively depicted on the vertical axis. The T_0 -line depicts the isotherm within the deposit corresponding to the first melting temperature and T_{70} depicts the isotherm corresponding to the flow temperature of the deposit. The figure is based on Backman et al. [18].

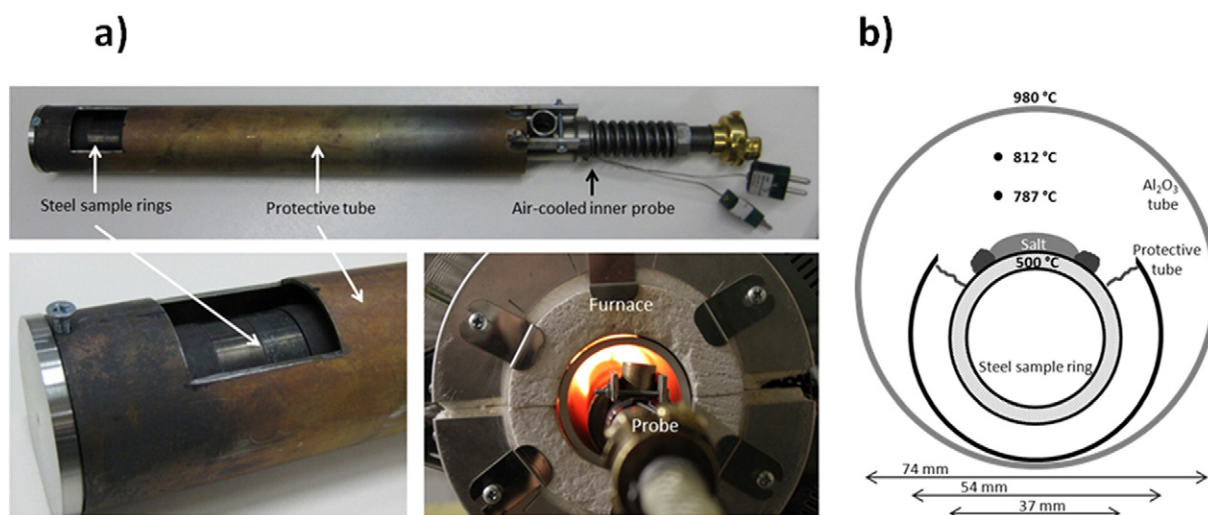


Fig. 2. a) Images of the corrosion probe and furnace. The length of the probe is about 60 cm. b) Schematic drawing of the cross-section showing setup arrangement and typical temperatures.

mixtures) and deposits from biomass-fired boilers, especially straw-fired boilers (KCl + K₂SO₄ mixtures). In addition, the changes in the chemical composition of the deposits due to the temperature gradients in the experiments were studied. Special attention was given to the vaporization/condensation of the alkali chlorides in the deposits. The effect of time on the changes of the deposit chemistry and morphology has also been studied. CFD-modeling has been utilized to model and interpret the vaporization/condensation phenomena. Due to the complex chemistry of superheater deposits in various types of boilers firing different fuels, the compositions of the synthetic deposit in the present study have been limited to binary KCl + K₂SO₄ and NaCl + Na₂SO₄ mixtures with known melting properties.

2. Experimental setup

The experimental setup in the present study is the same as the setup used by Lindberg et al. [29]. The main equipment used in the temperature gradient corrosion experiments is a corrosion probe placed into a tube furnace (Fig. 2). The corrosion probe consists of an inner probe placed in a protective tube, surrounding the inner tube except for a window exposing part of the steel sample rings to the furnace environment. The outer protective tube was mounted on the air-cooled probe in order to reduce the cooling effect from the probe, and hereby decrease the need for heating the tube furnace, resulting in more stable temperatures. The inner probe has two removable sample rings, which are equipped with thermocouples. The temperature of one of the test rings on the probe is regulated with a proportional-integral-derivative controller (PID controller) adjusting the flow of the cooling air. The temperature of the other test ring is monitored and logged during the test run. Tests were performed with the low-alloy steel 10CrMo9–10. Additional thermocouples can be installed on the outside of the protective tube to measure the temperature between the sample probe and the

Al₂O₃ tube in the furnace. The inner probe is the same as used by Bankiewicz et al. [30]. Fig. 2 shows images of the probe setup.

Synthetic deposits consisting of NaCl, Na₂SO₄, KCl, and K₂SO₄ were used in all experiments. To obtain homogenous salt mixtures, the components are mixed together, and the mixture are heated in a furnace, melted, and subsequently cooled to room temperature. The cooled mixture is crushed and sieved to a grain size fraction of 53–250 µm. The salt mixtures are then applied on each ring. Roughly 0.5 g of the salt mixture is applied on each ring. It corresponds to a thickness of about 5 mm of salt prior to the experiment. The edges of the rings are surrounded by a protective paste to maintain the salt in place in case of melting of the salts. For the experiments, the probe is inserted into a cold tube furnace and both the probe and the furnace are heated to their set temperatures. As stable temperatures are reached, the experiments run for 4, 24, or 72 h, and subsequently cooled to room temperature. After cooling, the salt deposits on the rings are cast in epoxy, and subsequently removed from the probe. The rings are cut and polished to get a cross-section of the ring and the salt deposit for SEM analysis. Fig. 2b shows a cross-section of the tube furnace and gradient test probe. An observation during the experiments is that the measured temperatures above salt deposit are considerably lower than the set temperature of the tube furnace. Fig. 2b also shows that the temperatures about 1 cm and 2 cm above the salt were measured as 787 °C and 812 °C, respectively, when the furnace temperature was set at 980 °C and the probe temperature was set at 500 °C.

The furnace temperature was set to 980 °C in all experiments presented in this paper. The probe temperature was set to 300, 400 °C or 500 °C. The measured temperatures in the furnace about one centimeter above the salt sample were about 780 ± 25 °C in the experiments. Experiments with the lower probe set temperature generally showed lower temperatures in the furnace but the exact position of the measuring thermocouple varied slightly between experiments, giving additional variations.

Table 1

Composition of salt mixtures used in the gradient furnace tests. Composition is given as actual salt mixture in weight percentage. The calculated and measured solidus temperatures (T_0) and liquidus temperatures (T_{100}) are also given.

Mixtures	Composition (wt.%)				Solidus temperature (°C)		Liquidus temperature (°C)	
	NaCl	Na ₂ SO ₄	KCl	K ₂ SO ₄	Calculated	Measured	Calculated	Measured
Eutectic Na ₂ SO ₄ –NaCl	32	68	–	–	626	627	626	627
Na ₂ SO ₄ -rich	6.4	93.6	–	–	626	624	818	Not measured
NaCl-rich	86.4	13.6	–	–	626	625	780	778
Eutectic K ₂ SO ₄ –KCl	–	–	55.5	45.5	690	685	690	685
K ₂ SO ₄ -rich	–	–	11.1	88.9	690	681	969	Not measured
KCl-rich	–	–	91.1	8.9	690	681	758	761

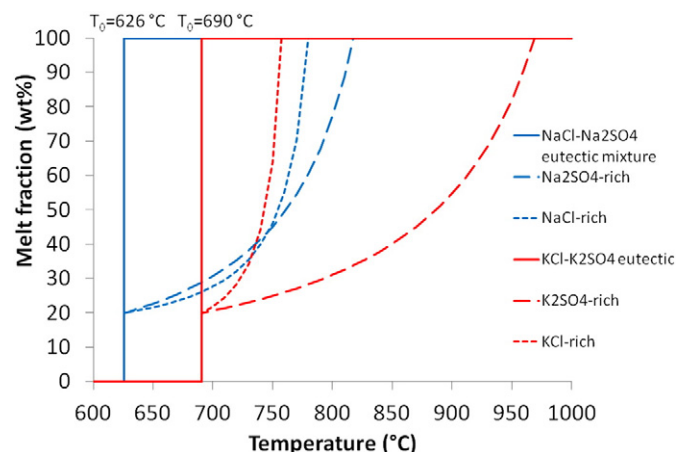


Fig. 3. Calculated melting curve of the NaCl + Na₂SO₄ and the KCl + K₂SO₄ mixtures. The solidus temperature (T_0) is 626 °C for the NaCl + Na₂SO₄ mixtures and 690 °C for the KCl + K₂SO₄ mixtures.

In the present study, different binary mixtures of NaCl + Na₂SO₄ and KCl + K₂SO₄ were used. One aim of the study was to investigate the effect of the melt fraction at the first melting temperature of the synthetic salt mixtures on the morphology of the deposit. A total of six different compositions were used in the present study. The mixtures were either eutectic mixtures, which means that the mixture will melt completely at the eutectic temperature, or mixtures with a melt fraction of 20 wt.% at the first melting temperature (solidus temperature). The mixtures with a melt fraction of 20 wt.% were either chloride-rich or sulfate-rich. The composition, measured and calculated melting temperatures of the six mixtures are given in Table 1, and the calculated melting curves for the mixtures are shown in Fig. 3. All thermodynamic calculations were made using the program Factsage [31] and the FTpulp database, which is based on the thermodynamic evaluation of the NaCl + Na₂CO₃ + Na₂SO₄ + KCl + K₂CO₃ + K₂SO₄ system by Lindberg et al. [4], where all experimental phase equilibrium and thermodynamic data for the were used as input for the optimization of the thermodynamic properties of the solid and liquid phases. The solidus temperature

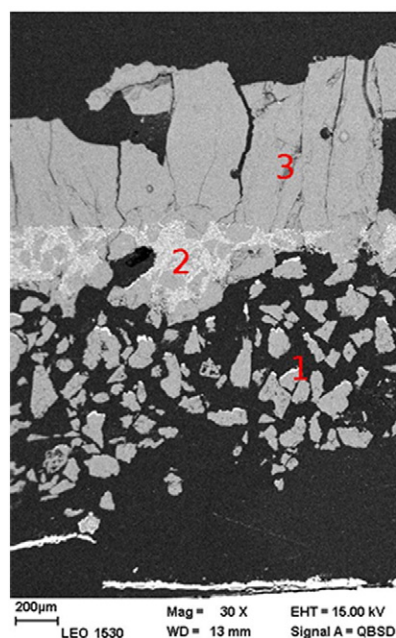
(first-melting temperature, T_0) and the liquidus temperature (complete melting temperature, T_{100}) of the salt mixtures were also measured using a TA Instruments Q600 Simultaneous DSC/TGA apparatus. The solidus temperature of the NaCl + Na₂SO₄ mixtures were close to 625 °C and for the KCl + K₂SO₄ mixtures around 685 °C. The measured solidus and liquidus temperatures correspond well with the calculated values.

All mixtures were run with the probe temperature at 500 °C and the furnace temperature set at 980 °C for 24 h. The Na₂SO₄-rich and K₂SO₄-rich mixtures were also run with the probe temperature at 300 °C, and 400 °C and 24 h, as well as with the probe temperature at 500 °C for 4 h and 72 h. The eutectic NaCl + Na₂SO₄ mixture has previously been studied at similar conditions with the probe temperature at 400 °C and 500 °C [29].

3. Experimental results

3.1. Deposit morphology

Scanning electron microscopy backscatter images of the cross-sections from the steel rings with the synthetic deposits showed that two or three distinct regions could be observed in the deposits. The thickness of the deposits was typically around 5 mm. A porous region was found closest to the steel surface, with sharp particle edges, suggesting no melting had occurred during the experiments and indicating that the region had only experienced temperatures below the solidus temperature (T_0). In the next region from the steel, the particles were observed to have agglomerated and sintered together. It was interpreted that the ash particles had been molten or partly molten during the experiment, indicating that the ash particles had experienced temperatures above T_0 . With the eutectic KCl + K₂SO₄ mixture, the KCl-rich mixture and all of the Na-mixtures, this region had a near eutectic composition. The third layer or region observed in the experiments was found farthest away from the steel surface. This region was sintered and agglomerated, indicating it had at some point of the experiment been molten or partly molten. The region consisted in almost every case of a single phase, which typically was the major solid phase of the original mixture. This region is referred to as the sintered region and it was observed in all of the experiments with non-eutectic mixtures.



Region	Temperature range	Properties
Sintered	T_0 – T_{furnace}	Sintered and agglomerated salt particles. Depleted of one component.
Eutectic	$\sim T_0$	Sintered and agglomerated. Eutectic composition.
Porous	T_0 – T_{steel}	Sharp particle edges. Bulk chemical composition is near the original. Pure alkali chloride layer were observed.

Fig. 4. A Scanning electron microscope back scatter image of a deposit cross-section showing three distinct regions and a table with region properties and temperature range. The porous region (1), the eutectic region (2) and the sintered region (3) were always observed in this order from steel to furnace.

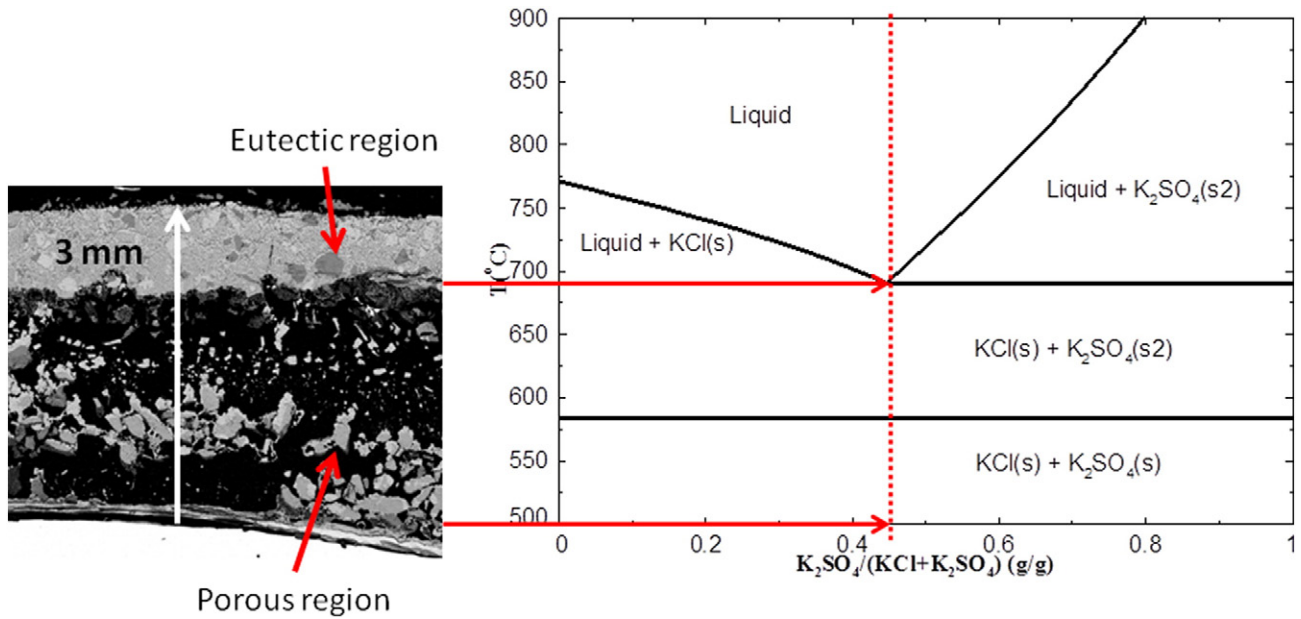


Fig. 5. A Scanning electron microscope backscatter image of a synthetic ash deposit cross-section with eutectic KCl + K₂SO₄ mixture and the binary phase diagram of KCl–K₂SO₄. The vertical red line in the phase diagram indicates the chemical composition of mixture. The horizontal arrows indicate the local chemical composition in the deposit at specific temperatures.

The eutectic mixtures exhibited only two regions, the porous region, corresponding with the original deposit mixture, and a completely sintered region, which exhibited a eutectic structure with sulfate and chloride crystals closely intertwined. The porous layer has in all cases been at temperatures below the first melting temperature of the mixture, whereas the sintered layer clearly shows signs that it has been close to completely molten during the experiments. The deposit morphology of the eutectic mixtures is explained with the melting behavior of the binary eutectic mixtures (Fig. 5). Below T_0 the particles were 100% solid and mostly retained their original form during the experiment. Above T_0 the particles were 100% molten and they agglomerated together forming a dense region with eutectic composition. Agglomeration was also observed in the porous region but it was considered to have occurred due to gas phase condensation of KCl or NaCl [29,32].

For non-eutectic mixtures, two or three regions were observed. For the K₂SO₄ rich mixture, only the porous and the sintered regions were observed in the deposit. In the rest of the non-eutectic mixtures, all three regions were observed (Fig. 6). The three regions were also observed in the 4 h experiment with the K₂SO₄ rich mixtures. The

deposit morphologies are explained with melting behavior of binary eutectic mixtures with accumulation of eutectic melt during melting of the deposit, leaving the major component as a solid at the top of the deposit. Below T_0 the particle edges are sharp and the deposit is not agglomerated. Above T_0 the particle edges are less sharp and the deposit is agglomerated and sintered.

The fact that eutectic regions were observed in synthetic deposits with non-eutectic mixtures suggests that the eutectic regions were formed during the experiment. In the experiments with Na₂SO₄ rich mixtures, the eutectic regions were enriched with NaCl. In addition the sintered regions were depleted of NaCl (Fig. 6). The results imply that NaCl was transported in the liquid phase towards the steel surface during the experiment. Depending on the exposure time, the sintered region was observed to be different. In the 4 h experiment, interstitial pockets containing NaCl + Na₂SO₄ with approximately eutectic composition were observed within the sintered region consisting of large Na₂SO₄ crystals. In the 24 and 72 h experiments with the same composition, similar eutectic areas were not observed in the sintered region. In the 4 h experiment, the separation of eutectic liquid and solid Na₂SO₄

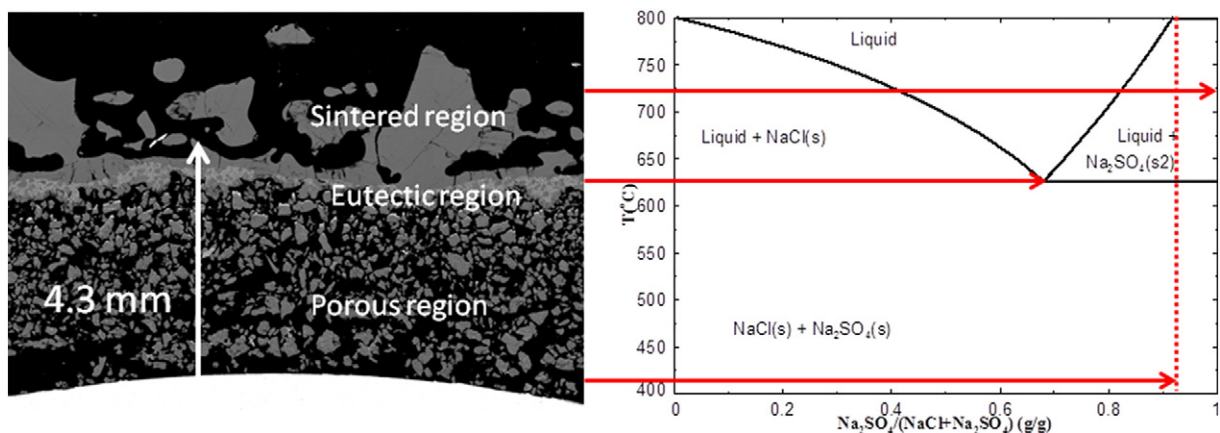


Fig. 6. Scanning electron microscope backscatter image of a synthetic ash deposit with Na₂SO₄ rich mixture and the binary phase diagram of NaCl–Na₂SO₄. The vertical red line in the phase diagram indicates the chemical composition of the mixture. The red arrows indicate the local chemical composition of the deposit in different temperature regions.

has been interrupted, whereas in the 24 h and 72 h experiments, the separation has gone to completion. The effect of time on the morphology of the sintered and eutectic regions is shown in Fig. 7.

The experiments with alkali chloride-rich mixtures showed similar behavior to experiments with Na_2SO_4 rich mixtures. The sintered region was uniform and depleted of K_2SO_4 or Na_2SO_4 and the eutectic region was enriched with K_2SO_4 or Na_2SO_4 with a near eutectic composition.

A eutectic region was observed in the 4 h experiment with the K_2SO_4 rich mixture but not in the other experiments with the same mixture. The overall cross-section and a detailed view of the eutectic region for the 4 h test is shown in Fig. 8. In the points A and B, areas with near eutectic composition were observed. In the points C and D, almost pure KCl layers were observed on top of the ash particles. The overall size of the agglomerated particle around point A is larger than the original ash particle size (250 μm). This implies that the agglomeration had taken place during the experiment and thus the eutectic region had also likely been formed during the experiment. On the basis of the presence of the eutectic region in the 4 h test, it is probable that similar regions had also been present in the 24 h and 72 h experiments with the K_2SO_4 rich mixture.

The molten phase transport in the $\text{KCl} + \text{K}_2\text{SO}_4$ system is similar to the $\text{NaCl} + \text{Na}_2\text{SO}_4$ system. The melt that is formed at temperatures above T_0 fills the void spaces between the original ash particles and is transported towards the steel surface. The transport into the void spaces is due to gravitational and capillary forces. Sharp shapes were observed within the eutectic region in most of the experiments with non-eutectic mixtures. An example is shown in Fig. 9. These shapes are similar to the particle shapes observed in the porous regions. Melt with eutectic composition can flow into the void spaces between the original particles. When the melt reaches an area where the temperature is below T_0 , it solidifies there.

In addition to the molten phase transport of compounds within the synthetic ash deposit, transport can also occur in the gas phase. Alkali sulfates have low volatility, suggesting that the enrichment of Na_2SO_4 or K_2SO_4 in the eutectic region of the alkali chloride-rich mixtures occurred only by molten phase transport. Alkali chlorides are more volatile than alkali sulfates. At 700 $^\circ\text{C}$, KCl has a calculated saturation pressure of $6.1 \cdot 10^{-5}$ bars and K_2SO_4 has a saturation pressure of $5.2 \cdot 10^{-10}$ bars. The high volatility of alkali chlorides enables the possibility for gas phase transport in the alkali sulfate-rich ashes. The absence of eutectic region in the 24 and 72 h experiments with the K_2SO_4 rich mixtures may be explained with the high volatility of KCl. The KCl in the eutectic region has the possibility to diffuse towards the steel or into the furnace. The sintered region in the experiments with K_2SO_4 -rich mixtures has a quite open skeletal morphology, which may allow part of the KCl to escape into the furnace (Fig. 8), whereas the

sintered region for the Na_2SO_4 -rich mixture is a massive, dense layer that is not easily penetrable by $\text{NaCl}(\text{g})$ molecules (Fig. 4, 6, 7, 9).

3.2. Deposit temperature gradient

Accurate determination of the temperature profile over the deposit is challenging due to the relatively thin deposit layer and steep temperature gradient. However, the temperature gradient over the porous region can be estimated based on the measured temperature of the steel ring and the solidus temperature (T_0) of the deposit.

It was assumed that the temperature at the steel–deposit interface was equal to the set temperature of the steel ring and that the temperature gradient over the porous region of the ash deposit was constant in the radial direction.

The temperature gradient through the porous region was calculated for all of the experiments with Eq. 1.

$$\frac{dT}{dx} = \frac{T_0 - T_{\text{steel}}}{x_{\text{porous}}} \quad (1)$$

where

$\frac{dT}{dx}$	is the temperature gradient over the porous region, [$^\circ\text{C}/\text{mm}$]
T_0	is the first melt temperature of the ash, [$^\circ\text{C}$]
T_{steel}	is the temperature of the steel surface, [$^\circ\text{C}$]
x_{porous}	is the thickness of the porous region, [mm]

The temperature gradient results are presented in Table 2.

It was observed that the sintered region–eutectic region interface followed the steel sample curvature. This implies that particles with the same radial distance from steel had experienced similar temperatures during the experiment.

Differences between the temperature gradient values over the porous region were observed in different experiments. Especially when comparing the values for the experiments with the K_2SO_4 rich mixture and the Na_2SO_4 rich mixture, differences can be observed. The experiments with the K_2SO_4 -rich mixture had an average temperature gradient of 58 $^\circ\text{C}/\text{mm}$ over the porous region while the experiments conducted with the Na_2SO_4 mixture had an average temperature gradient of 87 $^\circ\text{C}/\text{mm}$ over the porous region.

3.3. Alkali chloride layers in the porous region

Layers of pure NaCl or KCl were observed on the particles in the porous region in all of the experiments. The alkali chloride layers were observed on the surface of the particles facing the hotter region (upper

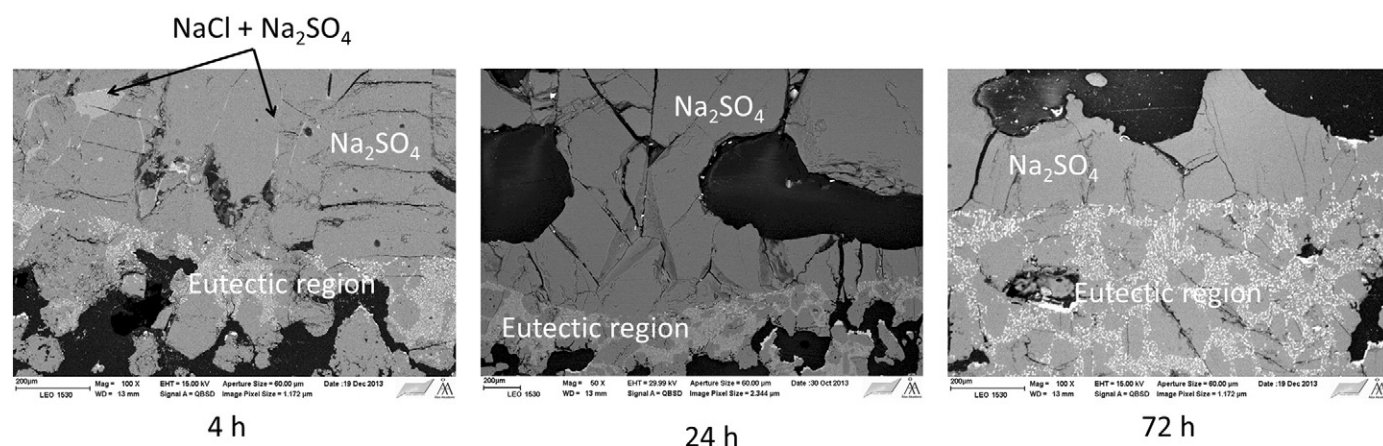


Fig. 7. Scanning electron microscope backscatter images of Na_2SO_4 -rich mixture cross-sections with different exposure times. The images show the eutectic and sintered regions. NaCl was observed in the sintered region in the 4 h experiment but not in the 24 and 72 h experiments. Na_2SO_4 is dark gray and NaCl is light gray.

surface of the particle). In all SEM images of the salt mixtures, the temperature increases in the vertical direction towards the top of the images. In some experiments, areas depleted in alkali chloride were observed on the particle surface facing the colder region, i.e. the steel surface. Scaffolds depleted of alkali chlorides were common in $\text{KCl} + \text{K}_2\text{SO}_4$ mixtures. In many cases, a layer consisting of small cubic crystals of NaCl or KCl was found on top of the oxide layer next to the steel surface. The diameter of the particles was typically less than $10\text{ }\mu\text{m}$, suggesting that they were formed during the experiments as the original material consisted of much larger particles. The existence of the alkali chloride crystals on the oxide surface can be considered as evidence that there is a gas phase transport of KCl and NaCl towards the colder parts in the porous region.

Alkali chlorides evaporate from the lower surface of the particles, then diffuse in the gas phase and deposit on the upper surface of the underlying particle or on the steel surface. Typical alkali chloride buildup layers and alkali chloride depleted areas are presented in Fig. 10.

The alkali chloride layer buildup was quantified for experiments with eutectic and sulfate-rich mixtures. The thickness of the alkali chloride layer on top of particles as well as the distance between the chloride layer and the steel surface was measured using the SEM images. The results with the Na_2SO_4 rich mixture show similar behavior with all of the tested steel temperatures. The thickest NaCl layers were found near the eutectic region and the thicknesses decreased towards the steel surface. However, the NaCl layers were found at different distances

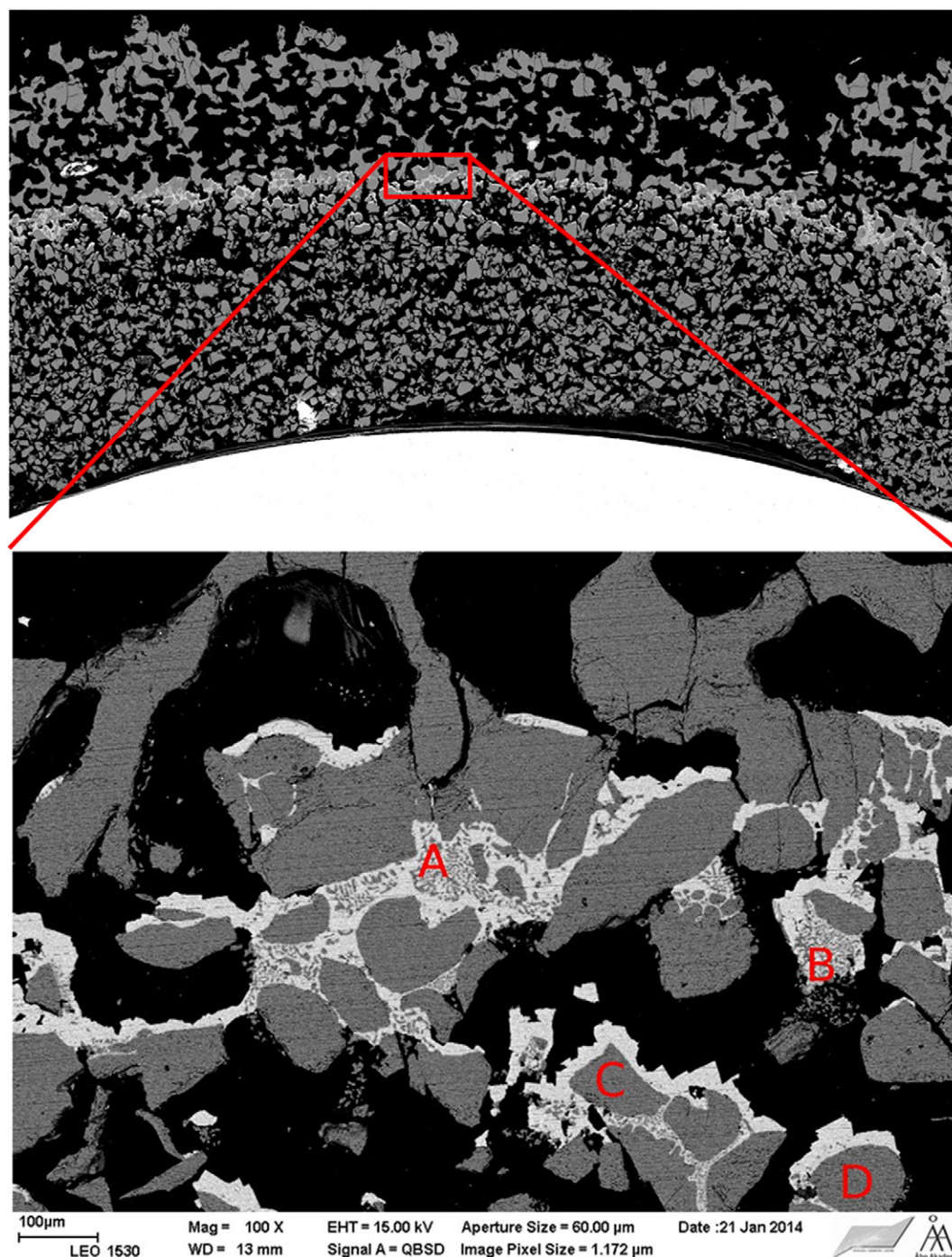


Fig. 8. Scanning electron microscope backscatter image of the 4 h experiment with the K_2SO_4 rich mixture. The top picture shows the overall cross-section and the lower picture shows a close-up of the eutectic region. The spots A and B have near eutectic compositions. On top of the particles C and D almost pure KCl layers were observed. K_2SO_4 is dark gray and KCl is white/light gray.

from the steel for different steel temperatures. The other mixtures showed similar behavior. The distance from steel surface was normalized to local temperature by using the temperature gradient values calculated in Table 2. Linear temperature dependence with distance from the steel surface was assumed. The results for the Na_2SO_4 rich mixture with different steel temperatures and exposure time of 24 h are shown in Fig. 11.

The results with different steel temperatures are similar when plotted against local temperature instead of distance. The alkali chloride buildup is dependent on the temperature. It was also observed that the deposit composition had a role in the alkali chloride layer formation. The KCl layer thickness results of experiments with KCl + K_2SO_4 mixtures with different steel temperatures and exposure time of 24 h are presented in Fig. 12. The KCl layers were noticeably thicker than the NaCl layers at a given temperature. At 600 °C the thicknesses of KCl layers were 10–150 μm and the thicknesses of NaCl layers were 10–25 μm . As will be discussed in more detail in Section 4, the reason for the thicker KCl layers is the greater mobility of KCl via intra-particle gas diffusion. KCl has higher saturation pressure than NaCl at temperatures between 300 and 700 °C.

The alkali chloride layers were thickest with the eutectic KCl + K_2SO_4 mixture. The KCl layers in the K_2SO_4 -rich mixture were slightly lower than for the eutectic mixture. It may be due to the fact that the sintered layer in the K_2SO_4 -rich mixture was slightly porous (Fig. 8), leading to KCl vaporization from the porous layer into the furnace. However, for the eutectic mixtures and the Na_2SO_4 -rich mixture, the escape of KCl or NaCl from the porous layer into the furnace was hindered by the compact eutectic and sintered layers.

The effect of time on the growth of the chloride layers is shown in Fig. 13. It can be seen that the NaCl layer in the Na_2SO_4 -rich mixture is the thickest for the 72 h experiment and the thinnest for the 4 h experiments for steel temperatures of 500 °C. However the growth rate does not seem to be linear as a function time, instead decreasing over time. Similar trends are seen for the K_2SO_4 -rich mixture, but the maximum values for the KCl layer thickness are roughly the same for the 24 h and 72 h tests up to about 630 °C. No KCl is observed above 630 °C for the 72 h test or above 670 °C in the 24 h test. A possible explanation is that the upper parts of the deposit layer is completely depleted of KCl in the longer experiments due to KCl transport towards the steel surface, as well as loss of KCl into the furnace. The lower maximum temperature for the KCl occurrence in the 72 h tests as well as the similar KCl layer thickness in the 24 and 72 h tests indicates that a loss of KCl has occurred in the 72 h sample compared to the 24 h sample.

The differences in saturation pressure of KCl and NaCl explain why the alkali chloride buildup in general is greater in the KCl + K_2SO_4 mixture compared to the NaCl + Na_2SO_4 mixture. In the Section 4, results from modeling of the gas phase transport of KCl and NaCl is discussed.

4. Modeling of alkali chloride transport

For analysis of the experimental observations of the alkali chloride buildup within the porous layer of the deposit, a model was developed using the computational fluid dynamics software Fluent as platform. The model considers a section of the deposit layer, with idealized positioning of the deposit particles. A typical calculation geometry is shown in Fig. 14.

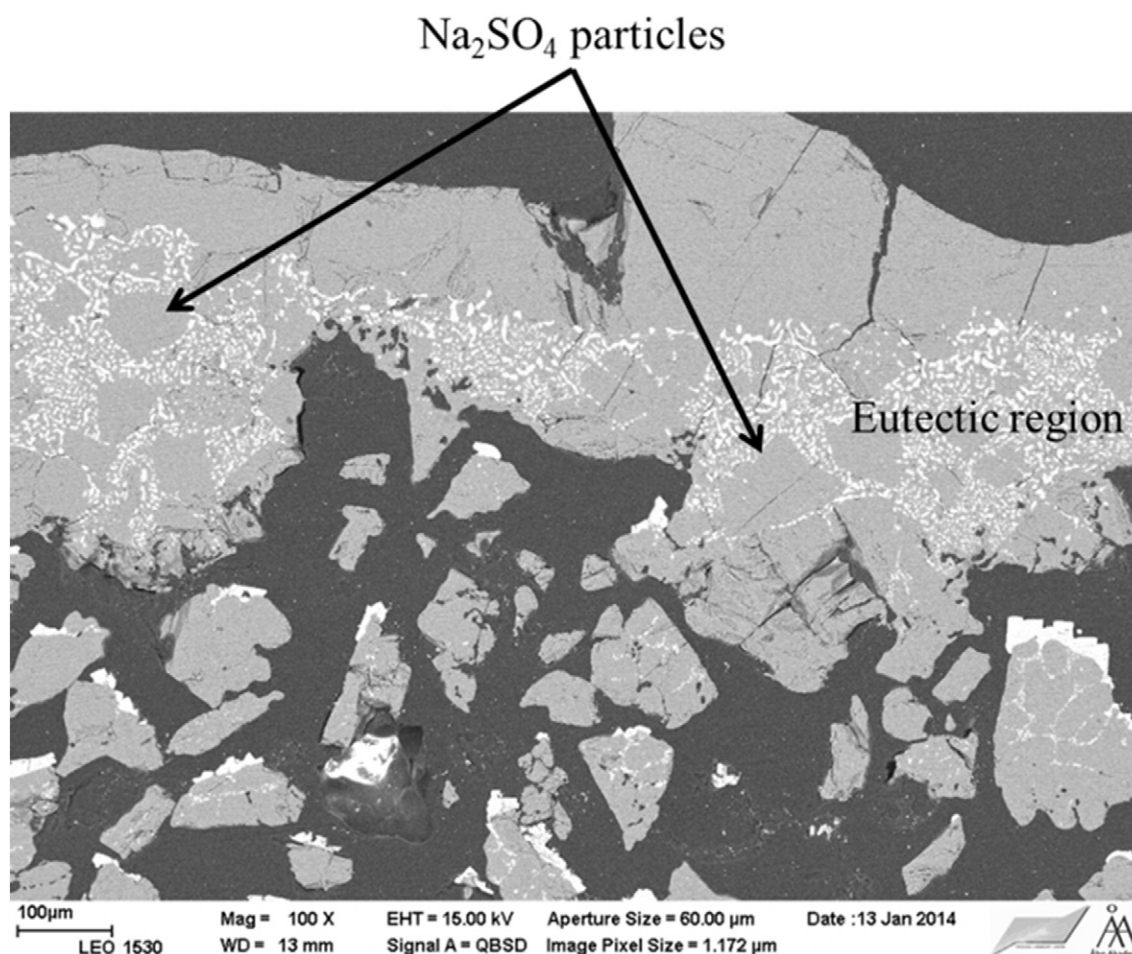


Fig. 9. A SEM image of the eutectic region in the 24 h experiment with the Na_2SO_4 rich mixture with steel temperature at 400 °C. Na_2SO_4 particles with sharp shapes were observed within the eutectic region. Na_2SO_4 is dark gray and NaCl is white/light gray.

The model predicts temperature profile of the considered deposit layer and the transport of alkali chloride within the void space between particles. The deposit layer temperature field is calculated by specifying (i) thermal conductivities of the salt and gas, 1 W/(m·K) and 0.05 W/(m·K), respectively, and (ii) temperature boundary conditions corresponding to the steel temperature and the temperature at the outer edge of the modeled region, where the eutectic temperature of the deposits was used: 626 °C and 690 °C for NaCl + Na₂SO₄ and KCl + K₂SO₄, respectively.

The modeled alkali chloride transport describes vaporization and condensation of alkali chloride vapor from and to the particle surfaces, respectively, as well as Fickian molecular diffusion transport of the vapor between the particles. A steady-state alkali chloride concentration field is solved considering Eq. (2), where the first term on the left is the diffusion term, and the second term is the source term.

$$\nabla \cdot (D_i \nabla \phi_i) + S_{\phi_i} = 0 \quad (2)$$

Fig. 15 presents an example of a calculated NaCl concentration field; along with the NaCl source terms for the same calculation case. Source terms for the alkali chloride species are calculated iteratively during solution in the near-particle cells by considering the concentration difference between each near-particle cell and the cell face representing the particle surface. Saturation pressure of the alkali chloride is assumed on

salt particle surfaces, and assuming ideal gas, used to calculate the alkali chloride concentration at each location on the particle surfaces. Equations for saturation pressures were fitted to thermodynamic equilibrium modeling results using the software Factsage [31]. NaCl and KCl form monomers and dimers in the gas phase: NaCl, (NaCl)₂, KCl, and (KCl)₂. The monomers are the dominating species in both cases. In the deposit layer model, the saturation pressures of the alkali chloride species are calculated using Eqs. (3)–(6).

Vaporization or condensation occurs depending on whether the gas phase alkali chloride concentration in the near-particle computational cell is below or above, respectively, the saturation concentration at the salt surface. Vaporization/condensation is calculated based on Fick's law of diffusion, with the condensation flux given by Eq. (7). Molecular diffusion coefficients used in the calculation of diffusive transport between salt particles as well as vaporization/condensation were based on the kinetic theory of gases; with molecule diameters estimated based on bond lengths and ionic radii [33]. The following molecule diameters were used in the model: NaCl = 0.378 nm, KCl = 0.427 nm, (NaCl)₂ = 0.578 nm, (KCl)₂ = 0.615 nm.

$$\log(P_{\text{NaCl}}^*) = -11795 \left(\frac{1}{T} \right) + 7.66 \quad (\text{pressure in bar, temperature in K}) \quad (3)$$

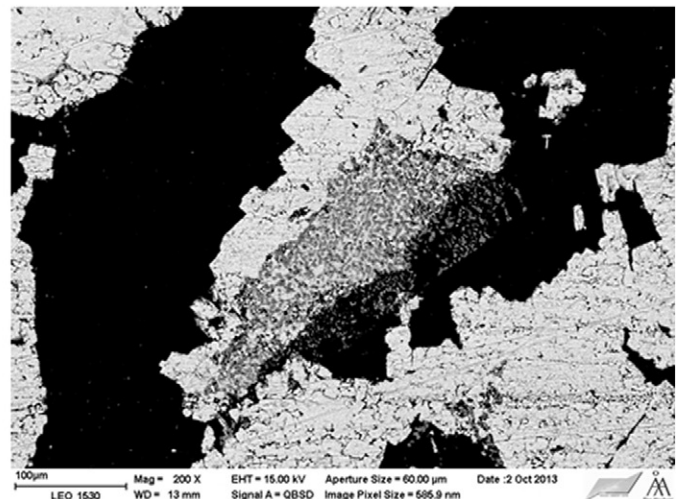
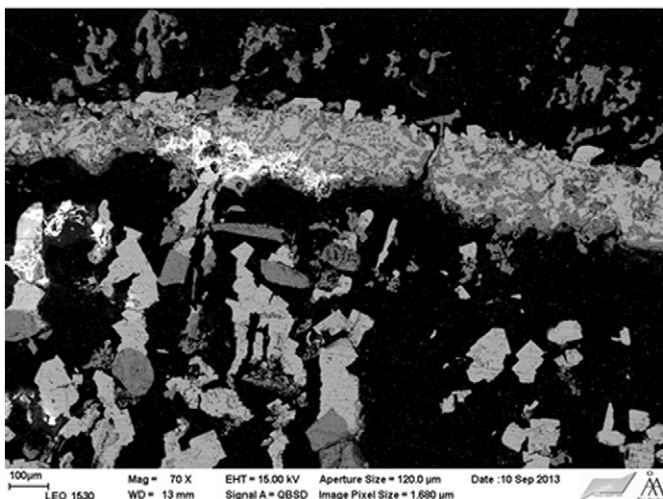
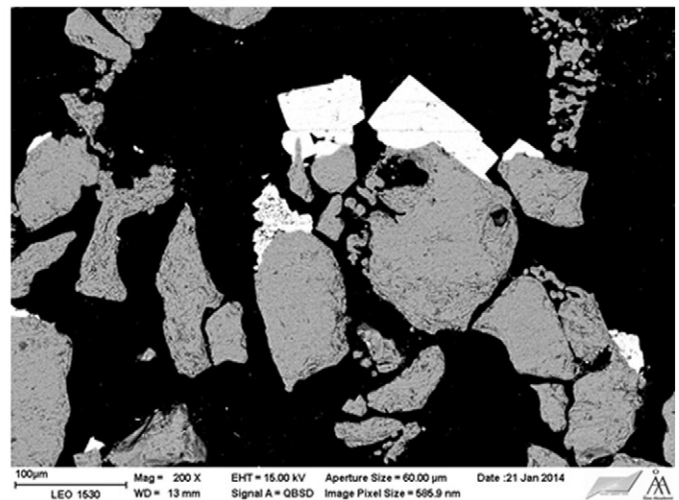
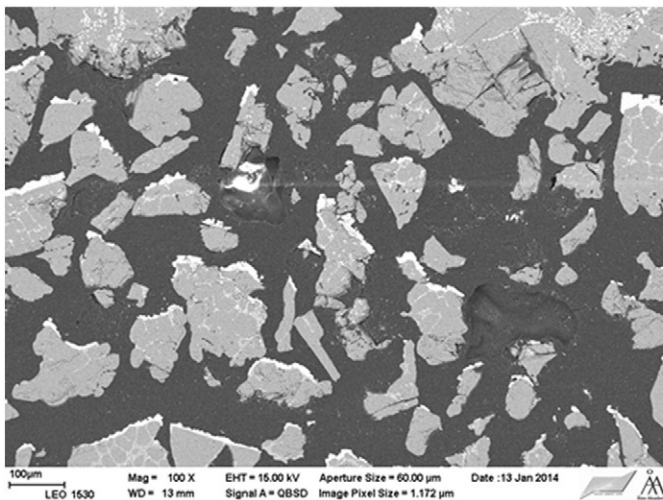


Fig. 10. Scanning electron microscope backscatter images showing the alkali chloride transport in the porous region. Transported NaCl layers (upper left), transported KCl layers (lower left and upper right) and particles with KCl depleted scaffolds (lower right). NaCl and KCl are the lighter phases in the figures.

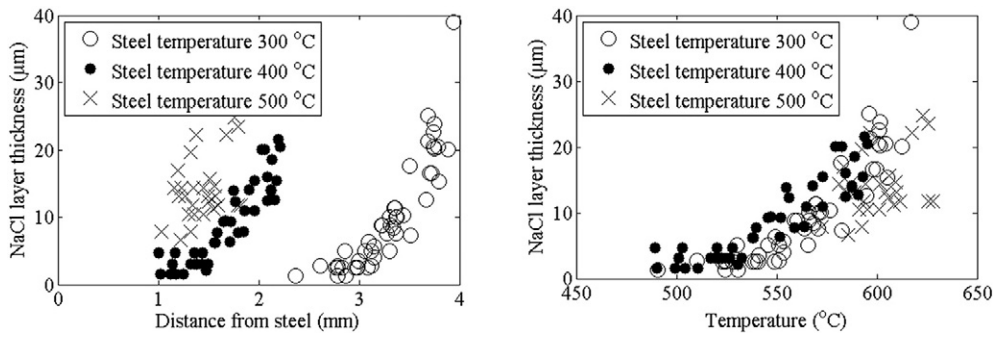


Fig. 11. NaCl layer thicknesses in the Na_2SO_4 rich mixtures plotted against the distance from steel (left) and the normalized local temperature (right). Experimental results are from tests with exposure time of 24 h and 300, 400, and 500 °C.

$$\log(P_{(\text{NaCl})_2}^*) = -13061\left(\frac{1}{T}\right) + 8.57 \quad (\text{pressure in bar, temperature in K}) \quad (4)$$

$$\log(P_{\text{KCl}}^*) = -11399\left(\frac{1}{T}\right) + 7.62 \quad (\text{pressure in bar, temperature in K}) \quad (5)$$

$$\log(P_{(\text{KCl})_2}^*) = -13054\left(\frac{1}{T}\right) + 8.95 \quad (\text{pressure in bar, temperature in K}) \quad (6)$$

$$J_i = D_i \frac{\Delta C_i}{\Delta x} \quad (7)$$

Fig. 16 presents model predictions of alkali chloride vaporization and depletion. The model shows vaporization and depletion to be greatest on the horizontal part of the salt particles, with the vaporization and condensation becoming zero at the vertical part of the salt particles. This prediction is in agreement with the observation from the experiments (Fig. 10), and is explained by the local temperature gradient being non-zero at the horizontal surfaces and zero at the vertical surfaces. The model further predicts vaporization and condensation rates to be dependent of the particle-to-particle distance: the closer the particles, the greater the vaporization and condensation rates. Due to the lower thermal conductivity of the gas, the temperature gradient over the particle-to-particle gas gap is greater as compared to that within a salt particle and greater than the global temperature gradient over the porous region. As shown in Fig. 16, the gas gap temperature gradient increases with particle-to-particle proximity resulting in increased vaporization and condensation rates. In the base case, the particle-to-particle distance corresponds to random close packing of hard-spheres [34].

Simulations were carried out representing the experimental conditions when using the $\text{KCl} + \text{K}_2\text{SO}_4$ and $\text{NaCl} + \text{Na}_2\text{SO}_4$ mixtures and steel temperatures of 400 °C and 500 °C. Salt layer thicknesses corresponding to the porous region (Table 2) were used. Fig. 17 presents model predictions of condensed alkali chloride layer thicknesses after 24 h. The thicknesses were calculated from the condensation rate in combination with alkali chloride densities of 2160 kg/m³ and 1980 kg/m³ for NaCl and KCl, respectively. Experimental alkali chloride layer thicknesses were the same as in Figs. 11 and 12. The agreement between the model predictions and the experimental data supports the hypothesis that the alkali chloride transport within the porous region is temperature gradient induced concentration diffusion. The model was tested by including thermal diffusion, but its contribution was found negligible compared to concentration diffusion. The greater transport rate of KCl as compared to NaCl is explained by the higher vapor pressure–temperature derivative dP^*/dT of KCl.

Several aspects should be considered in future modeling approaches, e.g. taking into account the change in porosity and the morphology of the porous layer as a function of time, more detailed determination of the transport properties of KCl and NaCl as well as their dimers $(\text{KCl})_2$ and $(\text{NaCl})_2$. Another aspect that should be considered is that the thickness growth rate is not constant as was suggested from the results shown in Fig. 13. However, the preliminary modeling results show promising results for explaining quantitatively the growth of the alkali chloride layers in the porous region of the deposit, as well as the difference between mixtures containing KCl or NaCl.

5. Conclusions and implications

The objective of the study was to investigate the effect of temperature gradients on the morphology and chemical composition of synthetic ash deposits relevant to biomass combustion. Synthetic ash deposits were applied on an air-cooled corrosion probe, which was inserted into a tube furnace. The effects of steel temperature, synthetic ash composition

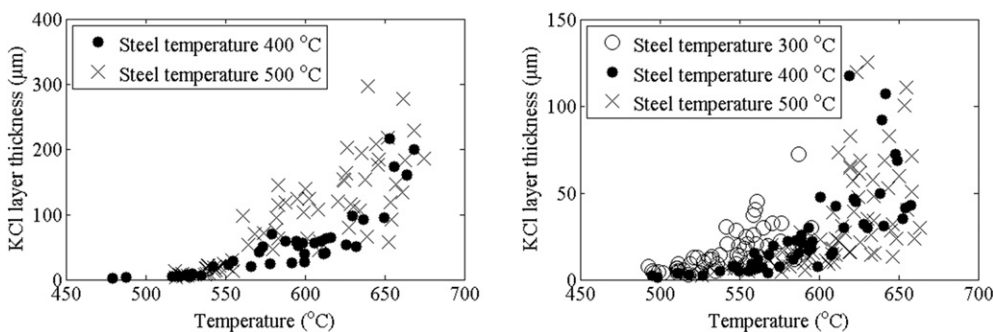


Fig. 12. KCl layer thicknesses in deposits with the eutectic $\text{KCl} + \text{K}_2\text{SO}_4$ mixture (left) and with the K_2SO_4 rich mixture (right) plotted against local temperature in the deposits. Experimental results are from tests with exposure time of 24 h and 300, 400, and 500 °C.

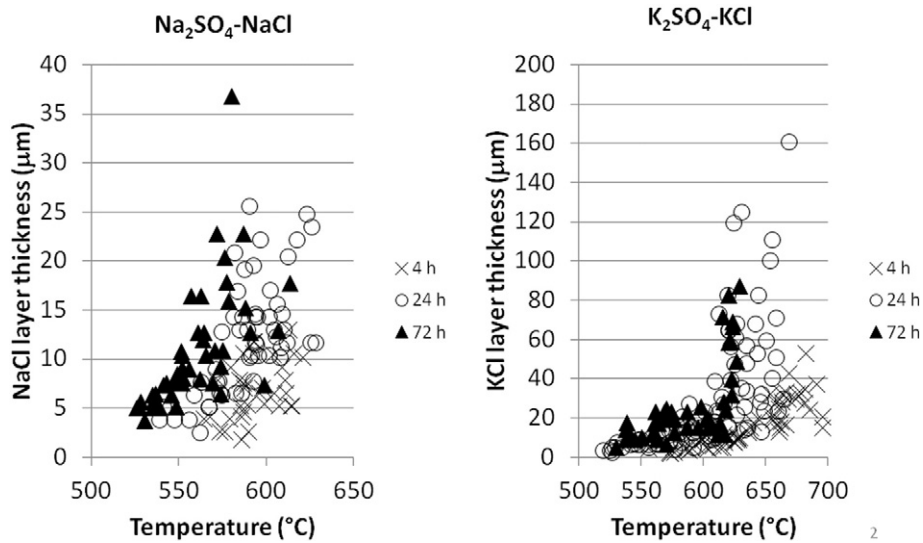


Fig. 13. NaCl layer thicknesses in the Na₂SO₄-rich mixture (left) and KCl layer thicknesses in the K₂SO₄-rich mixture (right) plotted against local temperature in the deposits at 4, 24, and 72 h and a steel temperature of 500 °C.

and exposure time were studied. In this study, steel temperatures of 300, 400 and 500 °C were used. The exposure times were 4, 24 and 72 h. The synthetic ashes were KCl + K₂SO₄ and NaCl + Na₂SO₄ mixtures with different ratios, simulating deposits found in straw-fired boilers and black liquor recovery boilers.

The temperature gradient was observed to have an effect on the deposit morphology. The presence of a temperature gradient led to a formation of different regions within the deposit. In experiments with ashes with eutectic composition, a region with porous morphology was observed closest to the steel. This region had the bulk chemical composition of the original ash. On top of the porous region there was

a region with compact morphology and eutectic composition. With non-eutectic mixtures, an additional region was observed on top of the compact eutectic region. This topmost region was sintered and depleted of the minor component of the ash. The eutectic and sintered regions were formed by complete or partial melting of the deposit and separation of the solid and liquid phase.

The temperature gradient also has an effect on the deposit chemistry in the porous region. The temperature gradient was observed to induce alkali chloride transport within the synthetic ash deposit. Alkali chlorides were observed to be transported towards the air-cooled steel surface. The phenomenon was modeled and the modeling results support the

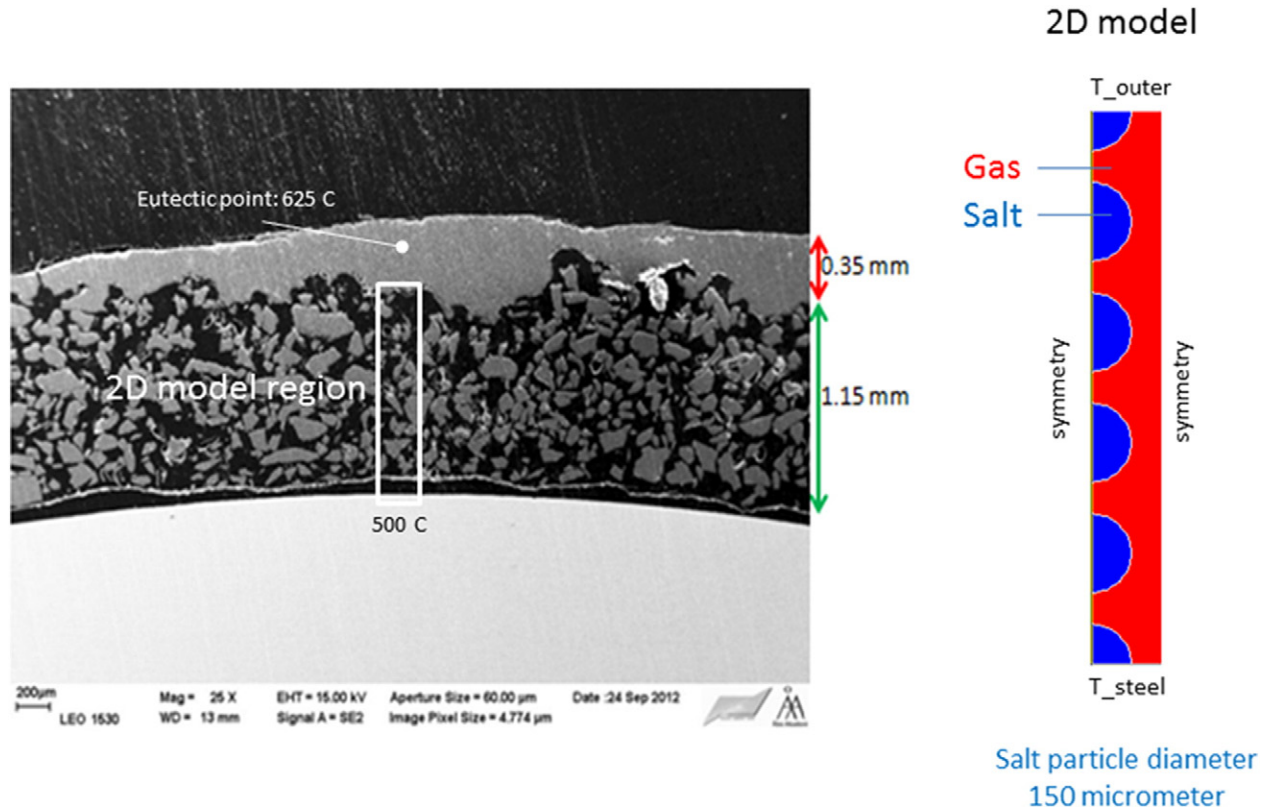


Fig. 14. Backscatter SEM image of a salt layer with a molten outer layer, and illustration of the modeling approach concerning geometry and temperature boundary conditions.

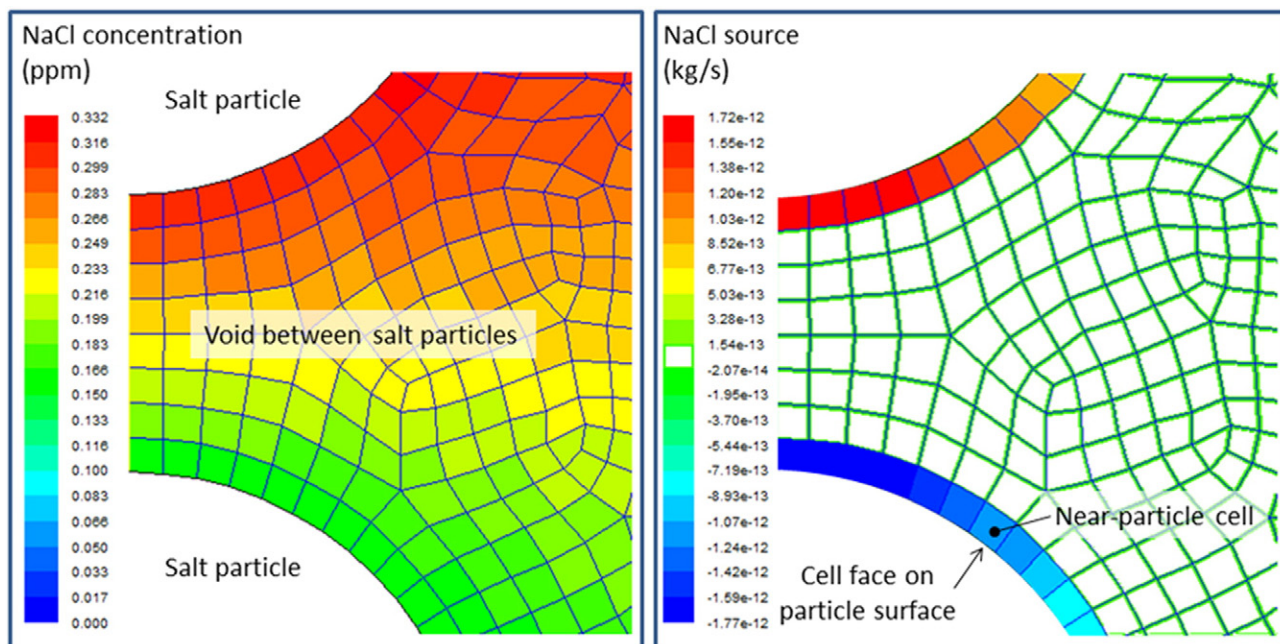


Fig. 15. Close-up of a section of the alkali chloride transport model geometry, shown are the calculation grid as well as NaCl(g) concentration (left) and NaCl(g) source terms (right).

hypothesis that the alkali chlorides are transported by gas phase diffusion. The temperature gradient induces an alkali chloride gas phase concentration gradient in the ash deposit. This leads to a gas phase diffusion of alkali chlorides towards the steel surface.

The morphologies observed in this study have similarities to real superheater deposits from biomass boiler. The alkali chloride layers on deposit particles observed in our experiments are similar to the 'KCl-fingers' reported by Hansen et al. [13] from a straw-fired boiler. Hansen et al. [13] speculated that the 'KCl-fingers' were formed by condensation and recrystallization of KCl or by thermophoresis of small

KCl particles. Our experimental observations and modeling results suggest that the condensation/recrystallization is a plausible explanation. Especially, the observations from eutectic KCl + K₂SO₄ mixtures, where columnar KCl layers are formed (Fig. 10), are very similar to 'KCl-fingers' of Hansen et al. [13]. Hansen et al. [13] and Jensen et al. [18] observed multilayer morphology of deposits rich in KCl and K₂SO₄, with porous regions that had not been molten and sintered regions that had clearly been molten at some stage.

In the porous region, NaCl and KCl were vaporized and condensed giving a net transport of NaCl and KCl towards the steel surface.

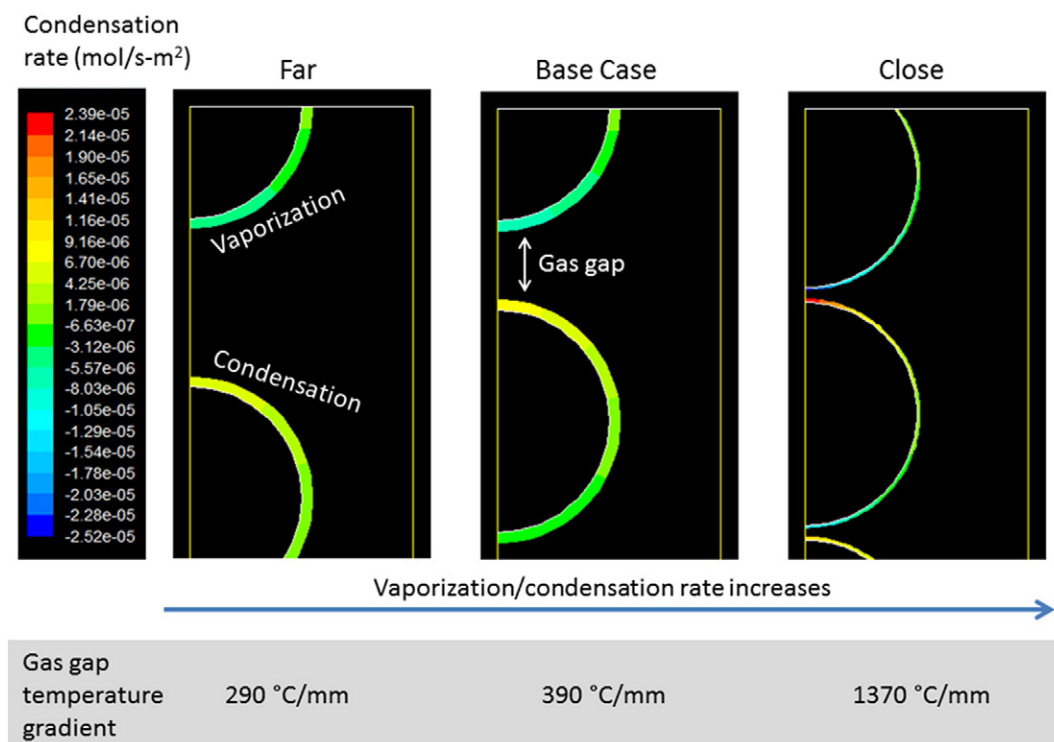


Fig. 16. Model predictions of NaCl vaporization and condensation using different particle-to-particle distances.

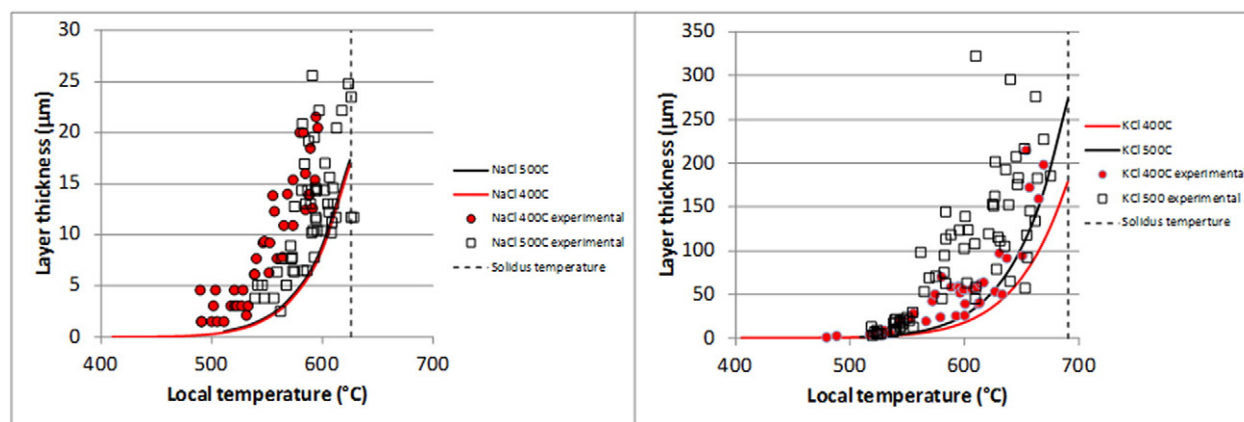


Fig. 17. Predicted alkali chloride thicknesses as a function of the local temperature inside the porous layer for 24 h compared with experimental results. Left graph shows results for NaCl + Na₂SO₄ mixtures and the right graph shows results for KCl + K₂SO₄ mixtures. The dashed vertical lines indicate the solidus temperature of the mixtures.

However, at lower temperatures the NaCl/KCl transport decreased. Therefore, for lower superheater temperatures, the transport of NaCl/KCl becomes less pronounced close to the steel surface. However, the transport of NaCl or KCl towards the steel surface can lead to enrichment of corrosive alkali chlorides on the steel surface. Especially superheater materials sensitive to chlorine-induced corrosion may get increased corrosion risks over time if NaCl or KCl is enriched on the steel surface. KCl showed larger vaporization/condensation tendencies than NaCl due to the higher saturation pressure of KCl. While the transport rate in an actual deposit most likely differs from the one in the experiments reported here, the model predictions indicate alkali chloride transport to the steel to strongly depend on steam temperature. Decreasing the steam temperature effectively decreases the potential for transport of chlorides to the deposit-steel interface and chlorine-induced corrosion.

The experimental procedure for the temperature gradient test is a novel approach with many untested parameters and conditions. Issues to be explored are for example the effect of the melt fraction at T_0 and how this will affect the overall deposit structure, more detailed models for the deposit layer thickness and the alkali chloride transport, initial particle size, and the effect of the probe/furnace geometry.

Acknowledgments

This work has been carried out within the Academy of Finland project “Behavior and properties of molten ash in biomass and waste combustion” (Decision no. 266384). The work has also been partly carried out

within FUSEC (2011–2014) as part of the activities of the Åbo Akademi Process Chemistry Centre. Other research partners are VTT, Lappeenranta University of Technology, Aalto University and Tampere University of Technology. Support from the National Technology Agency of Finland (Tekes), Andritz Oy, Metso (Valmet) Power Oy, Foster Wheeler Energia Oy, UPM-Kymmene Oyj, Clyde Bergemann GmbH, International Paper Inc. and Top Analytica Oy Ab is gratefully acknowledged (Tekes decision no. 235/11).

References

- [1] H.P. Nielsen, F.J. Frandsen, K. Dam-Johansen, L.L. Baxter, The implications of chlorine-associated corrosion on the operation of biomass-fired boilers, *Prog. Energy Combust. Sci.* 26 (2000) 283–298.
- [2] H. Tran, *Recovery boiler corrosion*, TAPPI Press, 1997 283–324.
- [3] M. Spiegel, Salt melt induced corrosion of metallic materials in waste incineration plants, *Mater. Corros.* 50 (1999) 373–393.
- [4] D. Lindberg, R. Backman, P. Chartrand, Thermodynamic evaluation and optimization of the (NaCl + Na₂SO₄ + Na₂CO₃ + KCl + K₂SO₄ + K₂CO₃) system, *J. Chem. Thermodyn.* 39 (2007) 1001–1021.
- [5] D. Lindberg, R. Backman, P. Chartrand, M. Hupa, A critical thermodynamic evaluation of the melting properties of alkali salt mixtures in the recovery boiler, 2007 International Chemical Recovery Conference, Paptac, Quebec City, QC, Canada 2007, pp. 47–50.
- [6] H. Tran, *Recovery boiler corrosion*, Kraft Recovery Boilers, Tappi Press, Atlanta, Georgia, USA 1997, pp. 283–324.
- [7] B.-J. Skrifvars, R. Backman, M. Hupa, K. Salmenoja, E. Vakkilainen, Corrosion of superheater steel materials under alkali salt deposits. Part 1: the effect of salt deposit composition and temperature, *Corros. Sci.* 50 (2008) 1274–1282.
- [8] B.J. Skrifvars, M. Westén-Karlsson, M. Hupa, K. Salmenoja, Corrosion of super-heater steel materials under alkali salt deposits. Part 2: SEM analyses of different steel materials, *Corros. Sci.* 52 (2010) 1011–1019.

Table 2

The global temperature gradients over the porous regions of the ash deposits and the parameters used to calculate the temperature gradients (T_0 , steel temperature and porous region thickness).

Mixture composition	Time (h)	Solidus temperature (°C)	Steel temperature (°C)	Thickness (mm)	Temperature gradient (°C/mm)
K ₂ SO ₄ –KCl eutectic	24	690	400	4.1	71
K ₂ SO ₄ –KCl eutectic	24	690	400	5.0	58
K ₂ SO ₄ –KCl eutectic	24	690	500	2.1	93
K ₂ SO ₄ –KCl eutectic	24	690	500	2.2	86
KCl-rich	24	690	500	3.6	53
K ₂ SO ₄ -rich	24	690	300	5.6	70
K ₂ SO ₄ -rich	24	690	400	4.9	59
K ₂ SO ₄ -rich	24	690	500	4.8	40
K ₂ SO ₄ -rich	24	690	500	2.8	68
K ₂ SO ₄ -rich	72	690	500	3.3	57
K ₂ SO ₄ -rich	4	690	500	3.6	53
NaCl-rich	24	626	500	2.2	57
Na ₂ SO ₄ -rich	24	626	300	3.5	92
Na ₂ SO ₄ -rich	24	626	400	2.3	100
Na ₂ SO ₄ -rich	24	626	500	1.8	69
Na ₂ SO ₄ -rich	24	626	500	1.5	84
Na ₂ SO ₄ -rich	72	626	500	1.8	68
Na ₂ SO ₄ -rich	4	626	500	1.2	106

- [9] H.J. Grabke, E. Reese, M. Spiegel, The effects of chlorides, hydrogen chloride, and sulfur dioxide in the oxidation of steels below deposits, *Corros. Sci.* 37 (1995) 1023–1043.
- [10] S.V. Vassilev, D. Baxter, L.K. Andersen, C.G. Vassileva, An overview of the chemical composition of biomass, *Fuel* 89 (2010) 913–933.
- [11] M. Zevenhoven, P. Yrjas, M. Hupa, Ash-forming matter and ash-related problems, in: M. Lackner, F. Winter, A.K. Agarwal (Eds.), *Handbook of Combustion Vol. 4: Solid Fuels*, WILEY-VCH Verlag GmbH & Co. KGaA, Weinheim 2010, pp. 495–531.
- [12] M. Zevenhoven, P. Yrjas, B.-J. Skrifvars, M. Hupa, Characterization of ash-forming matter in various solid fuels by selective leaching and its implications for fluidized-bed combustion, *Energy Fuel* 26 (2012) 6366–6386.
- [13] L.A. Hansen, H.P. Nielsen, F.J. Frandsen, K. Dam-Johansen, S. Horlyck, A. Karlsson, Influence of deposit formation on corrosion at a straw-fired boiler, *Fuel Process. Technol.* 64 (2000) 189–209.
- [14] H.P. Michelsen, F. Frandsen, K. Dam-Johansen, O.H. Larsen, Deposition and high temperature corrosion in a 10 MW straw fired boiler, *Fuel Process. Technol.* 54 (1998) 95–108.
- [15] M. Hupa, R. Backman, B.J. Skrifvars, M. Forssen, Liquor-to-liquor differences in combustion and gasification processes: dust composition and melting properties, *J. Pulp Pap. Sci.* 27 (2001) 416–422.
- [16] D. Lindberg, M. Becidan, L. Soerum, High efficiency waste-to-energy plants — effect of ash deposit chemistry on corrosion at increased superheater temperatures, *Energy Fuel* 24 (2010) 5387–5395.
- [17] D. Bankiewicz, P. Yrjas, D. Lindberg, M. Hupa, Determination of the corrosivity of Pb-containing salt mixtures, *Corros. Sci.* 66 (2013) 225–232.
- [18] P.A. Jensen, F.J. Frandsen, J. Hansen, K. Dam-Johansen, N. Henriksen, S. Hörlyck, SEM investigation of superheater deposits from biomass-fired boilers, *Energy Fuel* 18 (2004) 378–384.
- [19] R. Backman, M. Hupa, B.-J. Skrifvars, Predicting superheater deposit formation in boilers burning biomasses, *Impact of Mineral Impurities in Solid Fuel Combustion* 1999, pp. 405–416.
- [20] R. Backman, M. Hupa, E. Uppstu, Fouling and corrosion mechanisms in the recovery boiler superheater area, *TAPPI J.* 70 (1987) 123–127.
- [21] P. Isak, H.N. Tran, D. Barham, D.W. Reeve, Stickiness of fireside deposits in kraft recovery units, *J. Pulp Pap. Sci.* 12 (1986) J/84–J/88.
- [22] S.C. Okoro, M. Montgomery, F.J. Frandsen, K. Pantleon, High temperature corrosion under laboratory conditions simulating biomass-firing: a comprehensive characterization of corrosion products, *Energy Fuel* 28 (2014) 6447–6458.
- [23] J. Pettersson, H. Asteman, J.E. Svensson, L.G. Johansson, KCl induced corrosion of a 304-type austenitic stainless steel at 600 °C; the role of potassium, *Oxid. Met.* 64 (2005) 23–41.
- [24] J. Lagerbom, T. Lepisto, R. Backman, M. Hupa, Behavior of alkaline sulfate-chloride salts in temperature gradient corrosion test furnace, *VTT Symp.* 215 (2001) 541–551.
- [25] Y. Kawahara, Evaluation of high-temperature corrosion life using temperature gradient corrosion test with thermal cycle component in waste combustion environments, *Mater. Corros.* 57 (2006) 60–72.
- [26] J.M. Brossard, I. Diop, X. Chaucherie, F. Nicol, C. Rapin, M. Vilasi, Superheater fireside corrosion mechanisms in MSWI plants: lab-scale study and on-site results, *Mater. Corros.* 62 (2011) 543–548.
- [27] J. Frederick, W. James, A. Ling, H.N. Tran, S.J. Lien, Mechanisms of sintering of alkali metal salt aerosol deposits in recovery boilers, *Fuel* 83 (2004) 1659–1664.
- [28] T.R. Griffiths, N.J. Phillips, The determination of sorbet coefficients in molten salts by a new method using fiber-optic spectroscopy, *J. Electrochem. Soc.* 138 (1991) 3575–3581.
- [29] D. Lindberg, M. Engblom, P. Yrjas, J. Lindholm, T. Laurén, M. Hupa, Influence of deposit aging on superheater corrosion, 2014 International Chemical Recovery Conference, Tampere, Finland 2014, pp. 101–113.
- [30] D. Bankiewicz, E. Alonso-Herranz, P. Yrjas, T. Laurén, H. Spliethoff, M. Hupa, Role of ZnCl₂ in high-temperature corrosion in a bench-scale fluidized bed firing simulated waste wood pellets, *Energy Fuel* 25 (2011) 3476–3483.
- [31] C.W. Bale, E. Bélisle, P. Chartrand, S.A. Decterov, G. Eriksson, K. Hack, I.-H. Jung, Y.-B. Kang, J. Melançon, A.D. Pelton, C. Robelin, S. Petersen, FactSage thermochemical software and databases — recent developments, *Calphad* 33 (2009) 295–311.
- [32] M. Engblom, D. Lindberg, P. Yrjas, J. Niemi, T. Laurén, M. Hupa, Towards better understanding of temperature gradients in superheater corrosion, 11th International Conference on Fluidized Bed Technology, Beijing, China 2014, pp. 251–256.
- [33] K.S. Krane, *Modern Physics*, Wiley, 2012.
- [34] J.G. Berryman, Random close packing of hard spheres and disks, *Phys. Rev. A* 27 (1983) 1053–1061.